Opto-Electronic Advances

Original Article

2021, Vol. 4, No. 9

DOI: 10.29026/oea.2021.210017

Light-triggered interfacial charge transfer and enhanced photodetection in CdSe/ZnS quantum dots/MoS_2 mixed-dimensional phototransistors

Ziwei Li*, Wen Yang, Ming Huang, Xin Yang, Chenguang Zhu, Chenglin He, Lihui Li, Yajuan Wang, Yunfei Xie, Zhuoran Luo, Delang Liang, Jianhua Huang, Xiaoli Zhu, Xiujuan Zhuang, Dong Li and Anlian Pan*

Mix-dimensional van der Waals heterostructures (vdWHs) have inspired worldwide interests and efforts in the field of advanced electronics and optoelectronics. The fundamental understanding of interfacial charge transfer is of vital importance for guiding the design of functional optoelectronic applications. In this work, type-II 0D-2D CdSe/ZnS quantum dots/MoS_2 vdWHs are designed to study the light-triggered interfacial charge behaviors and enhanced optoelectronic performances. From spectral measurements in both steady and transient states, the phenomena of suppressed photoluminescence (PL) emissions, shifted Raman signals and changed PL lifetimes provide strong evidences of efficient charge transfer at the 0D-2D interface. A series of spectral evolutions of heterostructures with various QDs overlapping concentrations at different laser powers are analyzed in details, which clarifies the dynamic competition between exciton and trion during an efficient doping of 3.9×10^{13} cm^{-2}. The enhanced photoresponses (1.57×10^{4} $A\cdot W^{-1}$) and detectivities (2.86×10^{11} Jones) in 0D/2D phototransistors further demonstrate that the light-induced charge transfer is still a feasible way to optimize the performance of optoelectronic devices. These results are expected to inspire the basic understanding of interfacial physics at 0D/2D interfaces, and shed the light on promoting the development of mixed-dimensional optoelectronic devices in the near future.

Keywords: heterostructure; phototransistor; MoS_2; quantum dots

Li ZW, Yang W, Huang M, Yang X, Zhu CG et al. Light-triggered interfacial charge transfer and enhanced photodetection in CdSe/ZnS quantum dots/MoS_2 mixed-dimensional phototransistors. *Opto-Electron Adv* **4**, 210017 (2021).

Introduction

Low-dimensional heterostructures are extremely important members in various semiconductor devices, including photodetectors, phototransistors and light-emitting devices[1,2]. Recently, van der Waals heterostructures (vdWHs) based on 2D transition metal dichalcogenides (TMDs) have attracted world-wide attentions in the application of next-generation optoelectronic integrations

Key Laboratory for Micro-Nano Physics and Technology of Hunan Province, College of Materials Science and Engineering, School of Physics and Electronics, Hunan University, Changsha 410082, China.

*Correspondence: ZW Li, E-mail: ziwei_li@hnu.edu.cn; AL Pan, anlian.pan@hnu.edu.cn

Received: 8 February 2021; Accepted: 22 May 2021; Published: 25 September 2021

beyond traditional silicon-based integrated circuits[3,4]. Such 2D/2D vdWHs show unique properties, including high carrier mobility, atomic-scale depletion region and tunable light-matter interaction, which are stemming from the designed energy band alignment and the ultrafast interfacial charge transfer[5–7]. However, the interlayer coulomb interaction and the carrier scattering are dominant in such atomically-thin layers, which have great influences on the performance of optical behaviors and optoelectronic devices[8]. Besides, these kinds of devices still suffer from performance limitations due to their weak light absorption and pristine atom defects[9].

Several strategies have been devoted to tackle these problems, such as surface chemical modification[10,11], nanophotonic structures integration[12,13], mixed-dimensional vdWHs design[14], etc. The reduced dimension of semiconductors provides large specific surface areas and abundant interfaces, which means, TMDs flakes integrated with one-dimensional (1D) nanowires, especially with 0D quantum dots (QDs), could perform as promising architectures for high-performance optoelectronic devices[15–18]. To further achieve the high optoelectronic performance of mixed-dimensional vdWHs device, the integration of 2D materials with high carrier mobility and 1D or 0D materials with large light-sensitive absorption should be designed and fabricated. The reduced dimension creates abundant interfaces providing alternative channels to generate highly-efficient charge doping at the interface of 0D/2D semiconductors[19,20]. 0D QDs possess high quantum efficiencies, strong absorption coefficients, and low-cost processings, which are usually utilized to construct mixed-dimensional devices exhibiting broadband photodetection, excellent stability and remarkable photoresponsivity[21].

Molybdenum disulfides (MoS_2) monolayers are typical TMD semiconductors with band energy of 1.83 eV in visible spectral range, which usually show room temperature mobility of 0.1–10 $cm^2{\cdot}V^{-1}{\cdot}s^{-1}$, photoresponsivity of <10 $A{\cdot}W^{-1}$ and on-off ratios of 10^6–10^8 [22,23]. Perovskite QDs, such as $CH_3NH_3PbBr_3$ and $CsPbBr_3$, have recently been studied to build mixed-dimensional heterostructures with MoS_2 flakes showing enhanced optoelectronic responses[24–26]. But they face challenges in realizing air-stable heterostructures[27]. Besides, the design of heterostructure type among type-I and type-II is crucial, which decides carrier transfer behaviors and photoresponse enhancements[25,28]. Colloidal QDs and their core-shell QDs are stable semiconductors, which have been applied on MoS_2 layers to realize high-performance photodetectors[29,30]. Although these 0D/2D conceptual devices show outstanding performances in phototransistors and photodetectors, the charge transfer at the mixed-dimensional interfaces with complex ultrafast processes remains poorly understood[31–33]. Moreover, the light-controlled charge transfer processes in 0D/2D vdWHs have less been investigated, which may stimulate the design and creativity of photosensitive transistors.

In this work, we design 0D/2D mix-dimensional vdWHs (CdSe/ZnS QD/MoS_2) to investigate the light-triggered charge transfer processes at the nanoscale interface. The steady-state and transient-state optical measurements of colloidal QDs, MoS_2 monolayers and heterostructures are systematically investigated, showing tunable PL spectra and ultrafast charge transfer stemmed from a type-II band alignment. In a three-energy-level model, an effective charge transfer from QDs to MoS_2 monolayers can be verified from the weight ratio of exciton spectra, which has been estimated as 3.9×10^{13} cm^{-2}. The competition of QD exciton, MoS_2 exciton and trion can be further modulated in a light-triggered n-type doping process. Moreover, these power-sensitive charge transfer processes at the interface help to improve the performance of optoelectronic devices based on TMDs with large responsivities and detectivities. These results are expected to provide the fundamental understanding of light-triggered charge transfer in 0D/2D mixed-dimensional vdWHs, which will contributes to the designing of high-performance optoelectronic devices in the near future.

Materials and methods

Material preparation

MoS_2 monolayers were synthesized by chemical vapor deposition method. A quartz boat was filled with molybdenum oxide (MoO_3) powder and then located in the center of a furnace. The boat was covered by a cleaned Si/SiO_2 substrate. Another ceramic boat filled with sulfur (S) powder was placed at the upstream region of the furnace in a lower temperature zone. The temperature was raised to 830 °C for 10 min to grow MoS_2 crystals. Meanwhile, the S powder was heated to 300 °C by a heating belt, and the sulfur vapor flowed into the furnace by the carrier gas of Ar. Finally, the furnace was gradually cooled down to room temperature. During the whole process, the ultrahigh-purity Ar gas was held at 75 sccm

under atmospheric pressure. Colloidal CdSe/ZnS QDs are commercially available. The heterostructures were fabricated in a spin-coating process, where dilute solutions of 0.025 mg/L QDs can be spin-coated onto the MoS_2 monolayer at a rotation speed of 2700 rpm for 1 min.

Optial characterization

The optical properties were measured by a home-built μ-PL system. An iHR550 Raman spectrometer from Horiba was utilized to measure the PL and Raman spectra with 300 g·mm^{-1} and 1200 g·mm^{-1} gratings, respectively. A Ti: Sapphire laser at 400 nm (100 fs, 80 MHz) was used as the excitation source for transient-state measurements, which was generated by an 800 nm laser from a mode-locked oscillator (Tsunami 3941-X1BB, Spectra- Physics) positioned after a BBO crystal. Time-resolved PL (TRPL) is measured by a streak camera (Hasmamatsu Universal, C10910) with a resolution of ~3 ps for short-time range measurements (~200 ps). A 532 nm solid-state laser was also induced to excite samples to obtain the steady-state spectra. The objective lens is 50× magnifications, and the diameter of the laser spot is ~2 μm.

Device fabrication and measurement

The metal electrodes of MoS_2 and heterostructure devices were fabricated in a typical E-beam lithography (EBL) process, followed by e-beam evaporation of Au/Cr (100 nm/5 nm) electrodes. Then, samples were annealed in vacuum for 3 h at ≈180 °C to improve the contact conductance. The surface ligands of the coated QDs were purified by ethyl acetate and hexane to facilitate charge transport. Finally, the devices were annealed on a hot plate at 50 °C for 10 min to evaporate the solvent for electrical measurements. The electrical and optoelectronic properties of the as-fabricated devices were performed in a vacuum Lake Shore Probe Station combined with an Agilent B1500A semiconductor analyzer at room temperature.

Results and discussion

Figure 1(a) shows the schematic view of QD/MoS_2 heterostructures under the excitation of a laser. MoS_2 flakes were grown on SiO_2/Si substrate in a chemical vapor deposition (CVD) process. To fabricate mixed-dimensional 0D/2D vdWHs, a drop of solution with 0.025 mg·L^{-1} CdSe/ZnS QDs was then dropped onto a prepared CVD-grown $MoS_2/SiO_2/Si$ substrate. The density of QDs on substrates can be controlled by choosing the number of spin-coating times. From the optical images of pure MoS_2 flakes and 0D/2D vdWHs (Supplementary information S1), it can be obviously observed that the optical contrast of MoS_2 flakes varies when QDs are overlapped.

The structure and morphology of as-prepared QD/MoS_2 heterostructures can be confirmed by transmission electron microscopy (TEM) and atomic force microscopy (AFM). Figure 1(b) shows the high-resolution TEM image of MoS_2 monolayer. Our MoS_2 samples are of high-quality that there are no defects or substitute atoms observed from measurements. The inset shows the corresponding selected area electron diffraction (SAED) pattern. The pattern only presents one set of six-fold symmetry diffraction spots, which is stemming from the hexagonal atom arrangement of MoS_2 flakes. The enlarged high-resolution TEM (HRTEM) image is shown in Fig. 1(c), which is derived from the marked squares in Fig. 1(b). The interplanar spacing is measured to be 2.78 Å corresponding to (100) planes of hexagonal MoS_2. AFM topography of MoS_2 monolayer shows a clear triangular shape, and the thickness is determined to be 7.5 Å (1 Å=10^{-10} m).

After the wetting transfer process, QD/MoS_2 heterostructures can be successfully transferred onto the Cu grid. Figure 1(e) shows the low-resolution TEM image of QD/MoS_2 heterostructures, where QDs are randomly distributed on the surface of MoS_2 monolayer, which have been marked by the red arrows. The scale bar is 100 nm. From a HRTEM image with the scale bar of 20 nm, the diameters of QDs are ranging from 8–15 nm (Fig. 1(f) and Supporting Information S2). Notably, the wrinkles or the edges of MoS_2 monolayer are clearly observed as orange arrows point, which confirms that the as-transferred films are intact. From an enlarged area of HRTEM image of QD/MoS_2 heterostructure (Fig. 1(g)), Moiré patterns can be observed at the edge of QDs, which is caused by overlapping lattices between MoS_2 and QDs. The scale bar is 2 nm. The corresponding SAED image shows two different sets of arranged diffraction patterns, as shown in the inset of Fig. 1(g). The orange circles show a six-fold symmetry diffraction spots from MoS_2, while the red circles exhibit a parallelogram configuration from CdSe/ZnS QDs.

The optical and spectral properties have been investigated among CdSe/ZnS QDs, MoS_2 monolayers and their heterostructures. Figure 2(a) shows the UV-visible

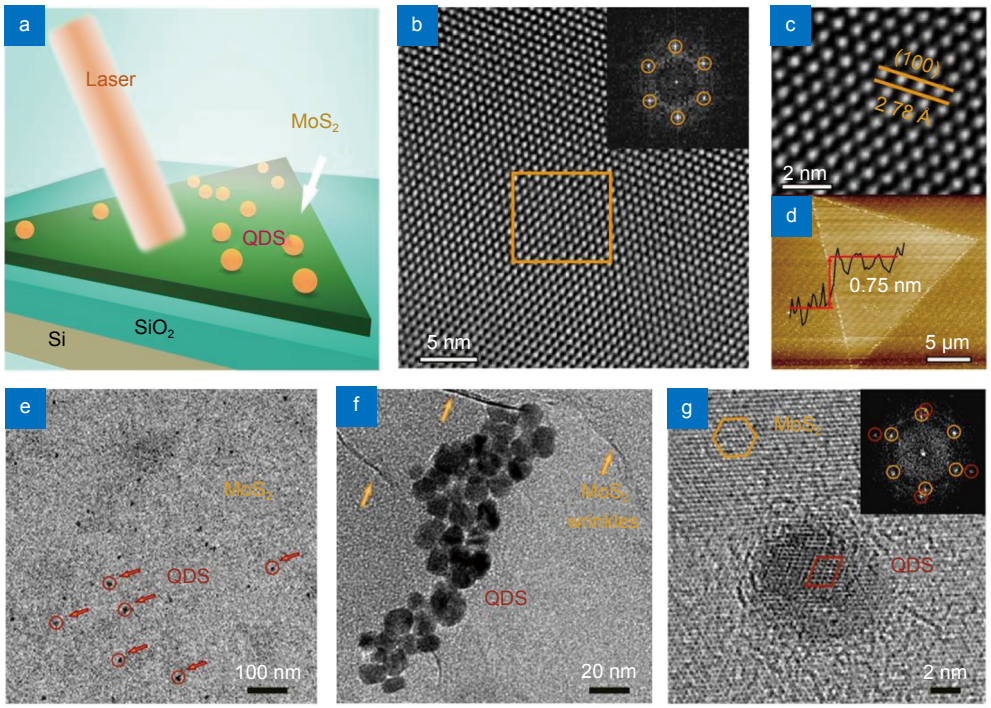

Fig. 1 | Schematic view and TEM characterizations of MoS_2 monolayer and CdSe/ZnS QDs. (**a**) Schematic view of mixed-dimensional QD/MoS_2 heterostructures on SiO_2/Si substrate under the excitation of a laser. (**b**) High-resolution TEM (HRTEM) image of MoS_2 monolayer with the scale bar of 5 nm. The inset shows the corresponding selected area electron diffraction (SAED) pattern, where the diffraction points are arranged in a hexagonal structure. (**c**) Enlarged FFT image of the marked area in a rectangular region in (b). The lattice spacing is 2.78 Å. (**d**) The AFM image of MoS_2 monolayer with clear surface, and the height of MoS_2 is observed to be 0.75 nm. Low-resolution (**e**) and high-resolution (**f**) TEM images of QD/MoS_2 heterostructures, where scale bars are 100 nm and 20 nm, respectively. The red arrows and circles in (e) are QDs on MoS_2 monolayer, and the orange arrows in (f) are the wrinkles of MoS_2 flakes. (**g**) The HRTEM image of QD/MoS_2 structures with a scale bar of 2 nm. Inset shows two sets of SAED patterns.

absorption spectrum of QDs solution, where two dominant absorption peaks are observed at around 450 nm and 620 nm. The PL spectra of QDs solution (0.2 mg·L^{-1}) and QDs film on SiO_2/Si substrate show Lorentzian lineshapes, where the peak center is 650 nm with a full width at half maximum (FWHM) of 45 nm. Although the excitation conditions are different, the PL spectrum of QDs on substrate exhibits a slightly-stronger spectral broadening than QDs in solutions. It is because of the change of the dielectric environment of exciton emissions.

Figure 2(b) shows the Raman spectra of MoS_2 monolayer (red curve) and QD/MoS_2 heterostructures (purple curve). Two typical Raman peaks of MoS_2 monolayer are observed at 384.2 cm^{-1} and 404.3 cm^{-1}, which correspond to the E^1_{2g} and A^1_g vibrational modes, respectively. The difference between these modes in the as-synthesized MoS_2 monolayer is approximately 20.1 cm^{-1}, which is slightly larger than the mechanically exfoliated monolayer MoS_2 because of the crystalline strain[34,35]. While in heterostructures, the Raman peaks of E^1_{2g} and A^1_g modes blue-shift lightly, which are arising from the strain force and the charge transfer at the interface of heterostructures. The peak intensity of heterostructures shows a great attenuation, which is due to the blocked signals by the overlapped QDs layer. Insets show two optical images of MoS_2 monolayer (left) and QD/MoS_2 heterostructures (right), and scale bars are 6 μm.

The absorption spectrum of MoS_2 monolayer is measured as shown in Fig. 2(c), which is derived from the differential reflectance spectra between MoS_2/substrate and substrate under white light illuminations. Two absorption peaks are observed to be located at approximately 622 nm and 659 nm, which correspond to direct excitonic transitions at K points in the Brillouin zone of MoS_2. Correspondingly, the PL spectrum of MoS_2 monolayer presents two featured peaks at 630 nm and 678 nm, respectively. In 0D/2D vdWHs, PL spectra show two peaks at 650 nm and 677 nm[14,36]. The peak intensity of exciton A decreases much, because charge transfer behaviors occurring at the interface suppress the radiative recombination. The PL spectra are excited by a 532 nm laser at 0.3 mW, and the detected samples are heterostructures with 0.025 mg·L^{-1} QDs.

PL intensity mapping has been performed to show spectral change in MoS_2 monolayer and heterostructures. Figure 2(d) and 2(e) show the images of PL mapping of MoS_2 monolayer at 665–750 nm and 640–660 nm, respectively, which are consistent with PL peaks of QDs and exciton A of MoS_2. It is obviously observed that the PL intensity is dominant at the spectral range of exciton A. Images of PL intensity mapping of vdWHs are shown in Fig. 2(f) (665–750 nm) and Fig. 2(g) (640–660 nm). In comparison to Fig. 2(d), the PL intensity of heterostructure in Fig. 2(f) decreases a little owing to the interfacial charge transfer, and the intensity distribution shows slight inhomogeneity. While at the detection wavelength of 640–660 nm, the intensity of heterostructure is slightly stronger than that of MoS_2 monolayer, where the intensity enhancement is mainly from the high-efficiency emission of QDs. Besides, a few QDs islands distributed on the substrate can also be observed. The laser powers are controlled at 0.3 mW for all the mapping measurements, and all the scale bars in Fig. 2(d–g) are 5 μm.

Time-resolved photoluminescence (TRPL) spectroscopy was carried out to further study and understand the spectral quenching caused by charge transfer. Fluorescence lifetime detection were obtained with 0.4 mg L^{-1} QD/MoS_2 samples excited by a pulsed laser (400 nm, 80 MHz), at an excitation power of 0.3 mW. The signals were subsequently filtered by 650/50 nm bandpass filters, which can collect the full PL spectral range of QDs while keeping away from the main PL peak of MoS_2 monolayer. The PL lifetimes for the two samples in Fig. 2(h) can be fitted and estimated using a biexponential decay model ($F(t) = \sum a_i e^{-(t-t_0)/\tau_i}, i = 1, 2$). The decay processes are considered to be consisted of fast decay τ_1 and slow decay τ_2. The fast decay is related to the trap-assisted recombination in QDs or carrier extraction by the layers in heterostructures, while the slow decay is related to radiative recombination[37,38]. By analyzing the components of two decay processes, the average lifetime of QDs and QD/MoS_2 heterostructures are determined to be 498.6 ps and 98.9 ps, respectively. The average lifetime of QD/MoS_2 heterostructure decreases much compared to QDs, indicating that considerable charge transfer can occur at the 0D/2D interface. Notably, the QDs in heterostructures exhibit a larger proportion of the fast decay than that exhibited by QDs alone, which confirms the trap-assisted recombination or carrier extraction is induced and dominant in QD/MoS_2 heterostructures due

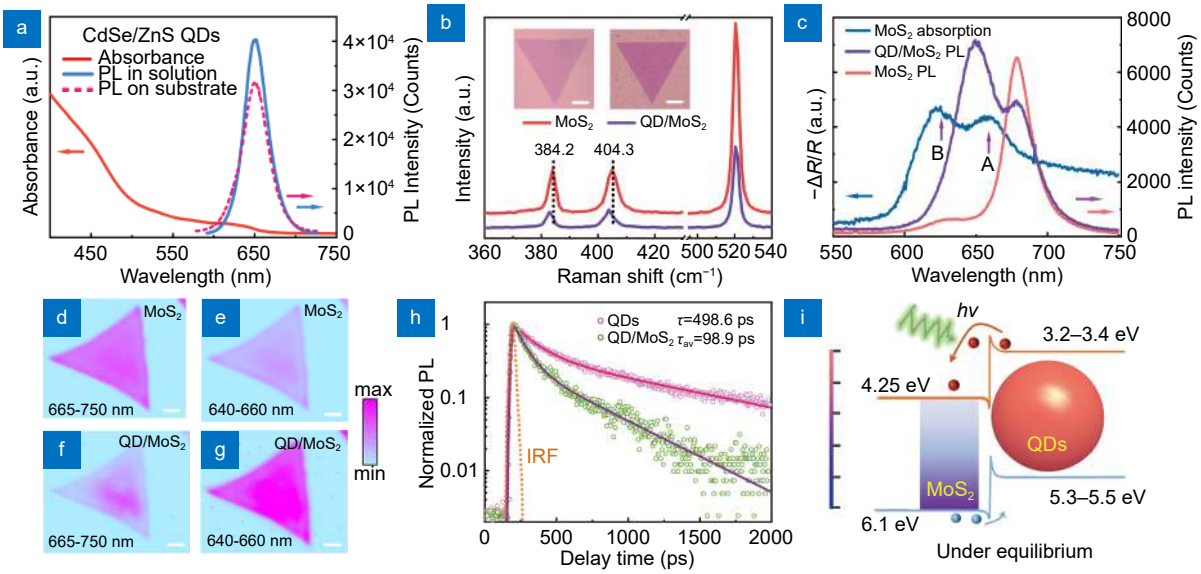

Fig. 2 | Optical and spectral characteristics of QDs, MoS_2 monolayer and mixed-dimensional vdWHs. (**a**) The UV-visible absorption spectrum (orange) of CdSe/ZnS QDs in 0.2 mg·L^{-1} solution. PL spectra of QDs in solution (blue) and on SiO_2/Si substrate (dotted line). (**b**) Raman spectra of MoS_2 monolayer and QD/MoS_2 heterostructures. E^1_{2g} and A_{1g} modes are 384.2 cm^{-1} and 404.3 cm^{-1} for MoS_2 monolayer, respectively, and the E^1_{2g} peak shifts blue to 383.3 cm^{-1} in heterostructures. Insets present the optical microscopy images of MoS_2 monolayer and heterostructure. The scale bars are 6 μm. (**c**) The absorption (black) and PL (red) spectra of MoS_2 monolayer. The PL intensity maps of MoS_2 monolayer are measured at the spectral ranges of (**d**) 665−750 nm and (**e**) 640−660 nm. The PL intensity maps of heterostructures with 0.025 mg·L^{-1} QDs are measured at the spectral ranges of (**f**) 665−750 nm and (**g**) 640−660 nm. All the scale bars in mapping images are 5 μm. (**h**) Time-resolved photoluminescence (TRPL) spectra of QDs and QD/MoS_2 heterostructures. The average lifetimes of QDs and heterostrutures are 498.6 ps and 98.9 ps, respectively. (**i**) The schematic view of energy band for QD/MoS_2 heterostructures under the light excitation.

to the charge transfer process (Supporting Information S3).

Figure 2(i) shows the energy band diagram of QD/MoS_2 heterostructures. The conduction band and valence band of MoS_2 monolayer are reported to be 4.25 eV and 6.1 eV in previous work, respectively[26]. While for QDs, the conductance and valence bands are reported to be 3.2–3.4 eV and 5.3–5.5 eV, respectively[39,40]. The energy band structure of QD/MoS_2 heterostructure is determined to be a type-Ⅱ band alignment. The built-in field is realized due to the interfacial charge transfer. With the excitation of incident laser, electron-hole pairs are mainly generated in the highly light-absorbing QDs layer, and then separated by the built-in field. As a result, electrons drift to the MoS_2 layer while holes are left in QDs.

To estimate the charge doping efficiency in heterostructures at various concentrations, the analysis of spectral evolution are performed to demonstrate the contribution of both exciton and trion in the PL spectra. Figure 3(a) shows the competition between exciton and trion emissions when the QD concentration is increased. At low concentrations, the exciton components are dominated in the total spectra, while the weight of exciton decreases as the concentration increases. All the components are fitted using Lorenze line-shaped peaks (Supporting Information S4).

The three-energy-levels model is shown in Fig. 3(b) to illustrate the competition between exciton and trion. Exciton is excited from the ground state to exciton energy level under the laser excitation (G). In an assumption that the trion is generated from the exciton in a non-radiative channel ($K_{tr}(n)$). Both the exciton ($\Gamma_{ex} = 0.002$ ps^{-1}) and trion ($\Gamma_{tr} = 0.02$ ps^{-1}) in MoS_2 monolayer generate PL signals in radiative channels. Then, the rate equations for the population of exciton (N_A) and trion ($N_{A'}$) can be expressed as

$$\frac{dN_A}{dt} = G - [\Gamma_{ex} + K_{tr}(n)]\,N_A, \tag{1}$$

$$\frac{dN_{A'}}{dt} = K_{tr}(n)N_A - \Gamma_{tr}N_{A'}, \tag{2}$$

$$K_{tr}(n) = K_{tr}(0)\left(1 - s\cdot\frac{1}{\alpha\cdot n + 1}\right), \tag{3}$$

where K_{tr} (n) is the formation rate of trion that relates with the QDs concentration (n), and K_{tr} $(0) = 0.5$ ps^{-1} is the formation rate of trion for the pure MoS_2 film[41]. The minimum k_{tr} (δ) can be obtained as 0.02 ps^{-1} as reported before. α is a parameter that reflects physical adsorption probability of QDs (Supporting Information S5)[42].

Figure 3(c) plots the changing trend of total PL intensity, exciton and trion at various concentrations. Both the

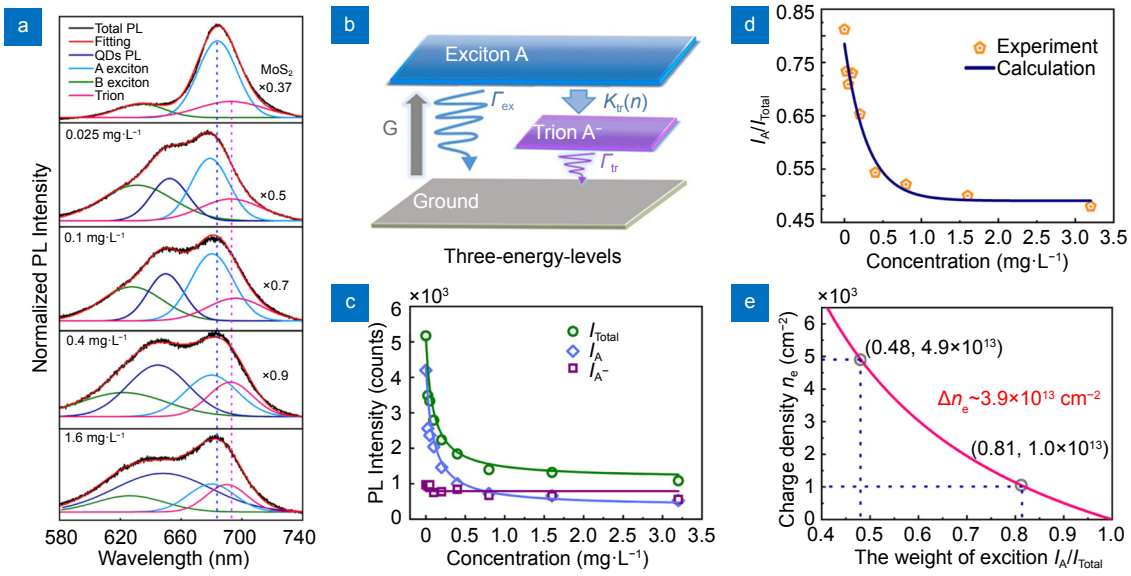

Fig. 3 | Analysis of PL spectral evolution of heterostructures at various doping densities. (**a**) Normalized PL spectra of QD/MoS_2 heterostructures with different QD concentrations. The total PL spectra (red) can be fitted well with several components, involving QD exciton (dark blue), MoS_2 exciton A (blue), trion (pink) and exciton B (green). (**b**) Schematic view of the three-energy-levels including exciton, trion and ground states, where the trion is generated from the exciton. (**c**) Diagram of PL intensity of total intensity (I_{Total}), exciton (I_A) and trion (I_{A^-}). Fitting curves match well with experimental results. (**d**) The weight ratio of exciton (I_A/I_{Total}) as a function of concentration. (**e**) Calculations of charge density (n_e) based on the law of mass action model. The electron density of charge transfer (Δn_e) is determined as 3.9×10^{13} cm^{-2}.

total PL intensity and the exciton intensity attenuate greatly as the concentration increases. Because the charge transfer electrons become abundant with high QDs concentrations, the recombination process of electron-hole pairs is deeply suppressed. However, the intensity of trion is almost unchanged in the doping process, which is due to the Pauli blocking effect and many-body interactions that the luminescence of the trion is easily saturated at low doping levels[43,44]. The weight ratio of exciton in total PL (I_A/I_{Total}) at different concentrations can be obtained from Fig. 3(c), where the ratio gradually decreases from 0.81 to 0.48 when the concentration increases, as shown in Fig. 3(d). Based on the mass action law, the charge density can be estimated from the weight ratio of exciton. Figure 3(e) shows the dependence of charge density with the weight ratio. The estimated charge density of MoS_2 monolayer is ~1×10^{13} cm^{-2} due to the vacancy-induced electron doping[45]. With 3.2 mg·L^{-1} QDs doping, the charge density of heterostructure can be calculated as 4.9×10^{13} cm^{-2}. Finally, the estimated density of doped electrons (Δn_e) is 3.9 × 10^{13} cm^{-2}, which confirms that n-type doping happens at the interface of QDs and MoS_2 (Supporting Information S6). Notably, this light-induced doping is at the same level of electric gating and chemical adsorption doping (~10^{13} cm^{-2})[46,47].

To further study the modulation ability of light-induced charge transfer and competitive exciton emissions, the laser-power dependent spectra of QDs, MoS_2 and heterostructures with 0.025 mg L^{-1} QDs have been systematically investigated. Figure 4(a) and 4(b) show power-dependent PL spectra of MoS_2 and QDs, respectively. When laser powers are increased from 65 to 670 μW, the intensity enhancement factors are determined as $P=I/I_0$, where I and I_0 are the intensities detected at high and low laser powers, respectively. P are detected as 8.4 for MoS_2 exciton A and 7 for trion, respectively (Supporting Information S7). While for QDs, the intensity enhancement factor is detected as 20, and peak positions are stably appearing at 650 nm.

Figure 4(c) shows the PL spectral evolution of QD/MoS_2 heterostructures with increasing laser powers ranging from 65 to 670 μW. There is an obvious competition between QD exciton (green), MoS_2 exciton A (blue) and trion (purple). At low power densities (<120 μW), MoS_2 exciton and trion emissions are dominant resulting in a higher PL intensity larger than QDs. When laser powers are further increased, all components of exciton

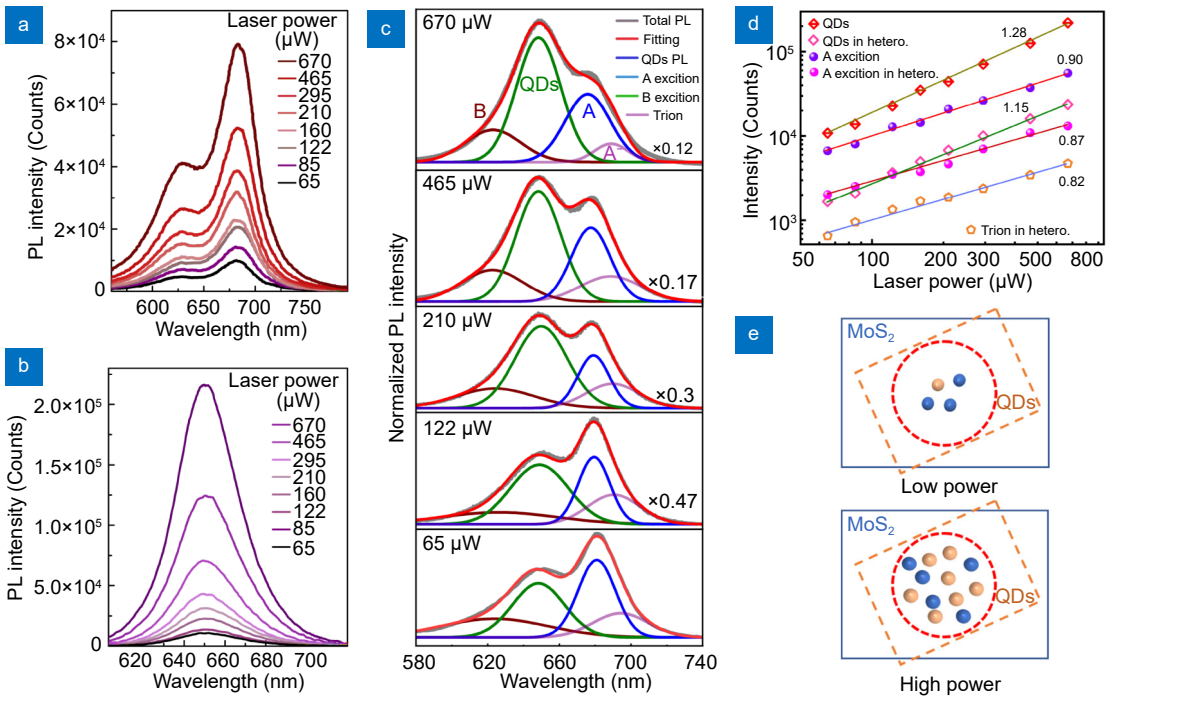

Fig. 4 | Laser-power dependent spectral modulation of QDs, MoS_2 and their heterostructures. PL spectra change of (**a**) MoS_2 monolayer and (**b**) QDs at various laser powers. (**c**) Analysis of PL spectral shapes in QD/MoS_2 heterostructure with the excitation of various laser powers. The total PL peak consists of QD exciton (green), MoS_2 exciton (A, blue), trion (A^-, purple) and B exciton, and they can be fitted well in the shape of Lorentzian curves. (**d**) Plots of normalized PL intensity of exciton and trion as a function of laser powers. The relationship of PL intensity (I) and laser power (P) can be fitted as $I=(P)^m$. (**e**) Schematic of exciton generation and emission at low and high laser powers.

and trion get stronger, but the increasement speed behaves differently. It can be observed that the component of QDs exciton increases much fast, which gets stronger and becomes comparable to the component of MoS_2 exciton at about 120 μW (Supporting Information S8).

The evolution of peak intensity of exciton and trion with laser powers has been plotted in Fig. 4(d). Both *x*-axis and *y*-axis are presented in log scales. The relationship of PL intensity (I) and laser power can be approximately written as $I=(P)^m$, where m denotes exponent. For QD exciton, m decreases from 1.28 to 1.15 (QDs exciton in heterostructures). The value of m obtained from exciton A of MoS_2 decreases from 0.9 to 0.87 (exciton A in heterostructures). The difference of PL sensitive-response gives rise to the competition and spectral evolution at various light powers. Figure 4(e) shows the schematics to illustrate the light-controlled spectral change. The blue rectangular and dotted orange rectangular show the areas of MoS_2 flakes and QDs films, respectively. In a QD/MoS_2 heterostructure with low QD density (as shown as the overlapping region), the number of MoS_2 excitons excited at low laser powers is larger than QDs excitons. However, when the laser powers are increased to a high level, more QD excitons are generated, which are comparable to the contribution of MoS_2 excitons, or even larger than that. The light-controlled spectral evolution shows the potential ability of tunable light-matter interactions in TMDs, which helps to influence the performance of optoelectronic devices.

The photo-induced charge behaviors are crucial to improve the performance of optoelectronic devices. The phototransistors of pristine MoS_2 and vdWHs are systematically investigated, and their characteristics of photocurrents are measured to investigate the influence of interfacial charge doping. Figure 5(a) shows the schematic view of the device, where MoS_2 monolayer served as a channel in the mix-dimensional FET (field-effect transistor), and Au/Cr (100 nm/5 nm) metal served as source/drain contacts on the back-gate Si/SiO_2 substrate. Under the light illumination, electrons from QDs are transferred into MoS_2 monolayer resulting in an efficient charge doping. The dilute solution of QDs can be uniformly spin-coated onto the MoS_2 monolayer to realize the mixed-dimensional vdWHs device.

To evaluate the optoelectronic performance of the vdWHs device compared to that of the MoS_2 transistor, we investigated the photo-induced transfer curves (Fig. 5(b)), as well as the current–voltage characteristics in the dark and under illuminations (Fig. 5(c)). Both pristine MoS_2 and hybrid phototransistors exhibit a typical n-type behavior in the dark. The threshold voltages of pristine MoS_2 and heterostructure phototransistors are obtained as −20 V and −60 V. As shown from the photoinduced transfer curves ($I_{ds}-V_g$) under the illumination (520 nm), I_{ds} of the photodetector in the dark is increased by ~4.8 times compared to that of the pristine MoS_2 device (7.55×10^{-7} A vs 1.56×10^{-7} A) at V_g=60 V. The enhanced drain currents (I_{ds}) under the illumination are obtained as 4.4 times for pure MoS_2 device (from 1.56×10^{-7} A to 6.86×10^{-7} A) and 11.3 times for QD/MoS_2 heterostructure device (from 7.55×10^{-7} A to 8.52×10^{-6} A) at V_g=60 V, respectively. It can be understood that the strong light absorption of QDs and the effective charge separation at the interface contribute to the amplified photocurrents in vdWHs devices. I_{ds} and V_g are the channel current and the gate voltage, respectively.

Furthermore, the photoresponsivity ($R=I_{ph}/P_{eff}$) and specific detectivity ($D^*=RS^{(1/2)}/(2eI_d)^{1/2}$) are calculated to investigate the device performance, where I_{ph} is the difference between photocurrent intensity and the dark-state current intensity, P_{eff} is the effective incident laser power ($P_{eff}=P_{in}\times S_{device}/S_{laserspot}$), S_{device} is the effective detection area of the device, I_d is the dark current, and e is the unit charge. Figure 5(d) and 5(e) show the calculated values of R and D^* as a function of P_{eff}, respectively, and the maximum values are detected at V_g = 60 V (the D^* versus V_g is presented in the Supporting Information S11). The calculated R of the hybrid device is enhanced by 21.4 times (from 733 $A\cdot W^{-1}$ to 1.57×10^4 $A\cdot W^{-1}$) compared to that of the pristine MoS_2 device, which is an outstanding performance compared to that of other TMD-based photodetectors (Supporting Information S12). Furthermore, the calculated R value exponentially increases as the incident power decreases due to the reduced scattering and recombination. The obtained highest D^* for the heterostructure device is enhanced by a factor of 9.6 compared to that of the pristine MoS_2 photodetector (from 2.98×10^{10} Jones to 2.86×10^{11} Jones).

We now discuss the possible mechanisms for improved photoresponsivities in these vdWHs devices. Both the photogating and photoconducting effects can coexist at the nanoscale interface, but the dominant mechanism varies. For the photoconductive effect, the current intensity linearly increases with excitation laser powers ($I\propto P_{eff}$), while it shows sublinear trend for

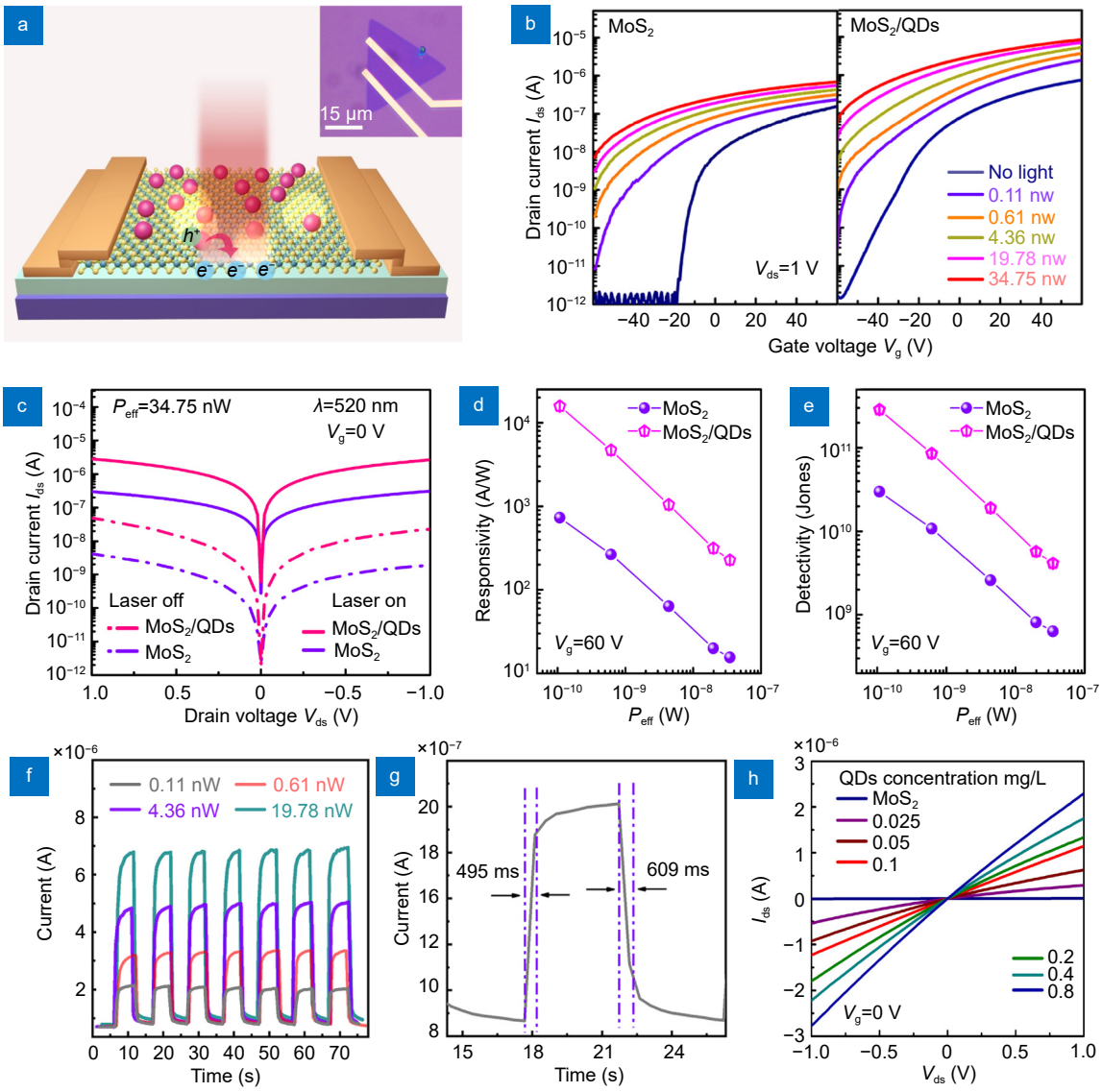

Fig. 5 | Optoelectronic performance of the vdWHs phototransistor compared with a pristine MoS_2 phototransistor. (**a**) Schematic view of the phototransistor device, and the inset is an optical image of the as-prepared device with the scale bar of 10 μm. (**b**) Transfer characteristics of two devices in the dark and under the illuminations (from 0.11 nW to 34.75 nW) at V_{ds}=1 V. (**c**) Transfer characteristics in dark (dotted line) and under the illumination (solid line, P_{eff} = 34.7 nW) at V_g=0 V. (**d**) Photoresponsivities and (**e**) specific detectivities of two devices as a function of effective powers at V_g=60 V, respectively. (**f**) Time-dependent photoresponses under the pulsed illumination powers (from 0.11 nW to 19.78 nW) over multiple cycles at V_{ds}=1 V. (**g**) The rise and fall times in photocurrent extracted from figure (f) under the illumination of 0.11 nW. (**h**) The photocurrent curves of vdWHs device with various QDs concentrations.

photogating effect ($I \propto P_{eff}^{\alpha}$ and α<1)[48,49]. The values of α at various V_g can be calculated and plotted as shown in Fig. S9 (Supporting Information S11), where α decreases from 0.78 to 0.26 (from −50 V to 60 V). It demonstrates that the main mechanism can be tuned from photoconducting to photogating effect by increasing the back-gate voltage.

Finally, the photoswitching characteristics of the hybrid photodetector are investigated under pulsed illumination powers over multiple cycles at V_{ds} = 1 V (Fig. 5(f)), and the rising time and the decay time extracted from the dynamic curves are shown in Fig. 5(g). Our mixed-dimensional photodetector exhibit stable and reproducible on-off photoswitching property, and the average rise and fall times are characterized to be 0.49 s and 0.6 s, respectively. Both the rise and fall curves in photocurrent can be fitted to a single exponential function. Figure 5(h) shows the I_{ds}–V_g curves of heterostructure devices overlapped with various QDs concentrations, where the photocurrent intensities (V_{ds}=1 V, V_g=0 V)

increases as the concentration increases. It confirms that the enhancement of light absorption from QDs can generate more photoinduced carriers and improve the detection photoresponsivity of devices.

Conclusions

In summary, we have demonstrated that interfacial charge transfer in 0D/2D mixed-dimensional vdWHs can be tailored and utilized to enhance the optoelectronic performance of phototransistors. A series of morphology characteristics and spectral measurements, including high-resolution TEM, AFM, Raman shift, suppressed fluorescence intensity, and short PL lifetime provide strong evidences to show type-II band alignment induced charge transfer. In a model of three-energy-levels, an effect photo-induced doping can be estimated as 3.9×10^{13} cm^{-2}, which contributes to the improved carrier mobility and enhanced optoelectronic performance of device in comparison with pure MoS_2 device (1.57×10^{4} $A\cdot W^{-1}$ vs 733 $A\cdot W^{-1}$, 2.86×10^{10} Jones vs 2.98×10^{10} Jones @520 nm) at a low power density (≈0.1 nW). Furthermore, the detuning of laser power and back-gate voltage provides an alternative way to manipulate the gain mechanism of device. Therefore, the interfacial control of charge transfer gives more freedoms to optimize the optoelectronic features of mixed-dimensional vdWHs, which may bring more opportunities for the coming atomic-level device integrations.

References

1. Zhang Z, Lin P, Liao QL, Kang Z, Si HN et al. Graphene-based mixed-dimensional van der Waals heterostructures for advanced optoelectronics. *Adv Mater* **31**, 1806411 (2019).
2. Jariwala D, Marks TJ, Hersam MC. Mixed-dimensional van der Waals heterostructures. *Nat Mater* **16**, 170–181 (2017).
3. Zeng QS, Liu Z. Novel optoelectronic devices: transition-metal-dichalcogenide-based 2D heterostructures. *Adv Electron Mater* **4**, 1700335 (2018).
4. Hu C, Dong DD, Yang XK, Qiao KK, Yang D et al. Synergistic effect of hybrid PbS quantum dots/2D-WSe_2 toward high performance and broadband phototransistors. *Adv Funct Mater* **27**, 1603605 (2017).
5. Song XF, Liu XH, Yu DJ, Huo CX, Ji JP et al. Boosting two-dimensional MoS_2/$CsPbBr_3$ photodetectors via enhanced light absorbance and interfacial carrier separation. *ACS Appl Mater Interfaces* **10**, 2801–2809 (2018).
6. Yang TF, Wang X, Zheng BY, Qi ZY, Ma C et al. Ultrahigh-performance optoelectronics demonstrated in ultrathin perovskite-based vertical semiconductor heterostructures. *ACS Nano* **13**, 7996–8003 (2019).
7. Li F, Feng YX, Li ZW, Ma C, Qu JY et al. Rational kinetics control toward universal growth of 2D vertically stacked heterostructures. *Adv Mater* **31**, 1901351 (2019).
8. Prins F, Goodman AJ, Tisdale WA. Reduced dielectric screening and enhanced energy transfer in single- and few-layer MoS_2. *Nano Lett* **14**, 6087–6091 (2014).
9. Lin Z, Carvalho BR, Kahn E, Lv RT, Rao R et al. Defect engineering of two-dimensional transition metal dichalcogenides. *2D Mater* **3**, 22002 (2016).
10. Bertolazzi S, Bonacchi S, Nan GJ, Pershin A, Beljonne D et al. Engineering chemically active defects in monolayer MoS_2 transistors via ion-beam irradiation and their healing via vapor deposition of alkanethiols. *Adv Mater* **29**, 1606760 (2017).
11. Nguyen DA, Oh HM, Duong NT, Bang S, Yoon SJ et al. Highly enhanced photoresponsivity of a monolayer WSe_2 photodetector with nitrogen-doped graphene quantum dots. *ACS Appl Mater Interfaces* **10**, 10322–10329 (2018).
12. Li ZW, Liu CX, Rong X, Luo Y, Cheng HT et al. Tailoring MoS_2 valley-polarized photoluminescence with super chiral near-field. *Adv Mater* **30**, 1801908 (2018).
13. Li ZW, Li Y, Han TY, Wang XL, Yu Y et al. Tailoring MoS_2 exciton-plasmon interaction by optical spin-orbit coupling. *ACS Nano* **11**, 1165–1171 (2017).
14. Ying HT, Li X, Wang HM, Wang YR, Hu X et al. Band structure engineering in MoS_2 based heterostructures toward high-performance phototransistors. *Adv Opt Mater* **8**, 2000430 (2020).
15. Hou HL, Zhang XW. Rational design of 1D/2D heterostructured photocatalyst for energy and environmental applications. *Chem Eng J* **395**, 125030 (2020).
16. Konstantatos G, Badioli M, Gaudreau L, Osmond J, Bernechea M et al. Hybrid graphene–quantum dot phototransistors with ultrahigh gain. *Nat Nanotech* **7**, 363–368 (2012).
17. Zheng DS, Wang JL, Hu WD, Liao L, Fang HH et al. When nanowires meet ultrahigh ferroelectric field−high-performance full-depleted nanowire photodetectors. *Nano Lett* **16**, 2548–2555 (2016).
18. Luo WJ, Weng QC, Long MS, Wang P, Gong F et al. Room-temperature single-photon detector based on single nanowire. *Nano Lett* **18**, 5439–5445 (2018).
19. Kufer D, Lasanta T, Bernechea M, Koppens FHL, Konstantatos G. Interface engineering in hybrid quantum dot–2D phototransistors. *ACS Photonics* **3**, 1324–1330 (2016).
20. Bessonov AA, Allen M, Liu YL, Malik S, Bottomley J et al. Compound quantum dot-perovskite optical absorbers on graphene enhancing short-wave infrared photodetection. *ACS Nano* **11**, 5547–5557 (2017).
21. Kagan CR, Lifshitz E, Sargent EH, Talapin DV. Building devices from colloidal quantum dots. *Science* **353**, aac5523 (2016).
22. Wang HM, Li CH, Fang PF, Zhang ZL, Zhang JZ. Synthesis, properties, and optoelectronic applications of two-dimensional MoS_2 and MoS_2-based heterostructures. *Chem Soc Rev* **47**, 6101–6127 (2018).
23. Subbaiah YPV, Saji KJ, Tiwari A. Atomically thin MoS_2: a versatile nongraphene 2D material. *Adv Funct Mater* **26**, 2046–2069 (2016).
24. Cheng YC, Li HJW, Liu B, Jiang LY, Liu M et al. Vertical 0D-perovskite/2D-MoS_2 van der Waals heterojunction phototransistor for emulating photoelectric-synergistically classical pavlovian conditioning and neural coding dynamics. *Small* **16**, 2005217 (2020).

25. Wu HL, Kang Z, Zhang ZH, Zhang Z, Si HN et al. Interfacial charge behavior modulation in perovskite quantum dot-monolayer MoS_2 0D-2D mixed-dimensional van der Waals heterostructures. *Adv Funct Mater* **28**, 1802015 (2018).
26. Wu HL, Si HN, Zhang ZH, Kang Z, Wu PW et al. All-inorganic perovskite quantum dot-monolayer MoS_2 mixed-dimensional van der Waals heterostructure for ultrasensitive photodetector. *Adv Sci* **5**, 1801219 (2018).
27. Zhang LW, Shen SL, Li M, Li LY, Zhang JB et al. Strategies for air-stable and tunable monolayer MoS_2-based hybrid photodetectors with high performance by regulating the fully inorganic trihalide perovskite nanocrystals. *Adv Opt Mater* **7**, 1801744 (2019).
28. Luo P, Zhuge FW, Wang FK, Lian LY, Liu KL et al. PbSe quantum dots sensitized high-mobility Bi_2O_2Se nanosheets for high-performance and broadband photodetection beyond 2 μm. *ACS Nano* **13**, 9028–9037 (2019).
29. Tang X, Lai KWC. Graphene/HgTe quantum-dot photodetectors with gate-tunable infrared response. *ACS Appl Nano Mater* **2**, 6701–6706 (2019).
30. Nikitskiy I, Goossens S, Kufer D, Lasanta T, Navickaite G et al. Integrating an electrically active colloidal quantum dot photodiode with a graphene phototransistor. *Nat Commun* **7**, 11954 (2016).
31. Liu H, Wang C, Wang T, Hu XM, Liu DM et al. Controllable interlayer charge and energy transfer in perovskite quantum dots/transition metal dichalcogenide heterostructures. *Adv Mater Interfaces* **6**, 1901263 (2019).
32. Zhang SK, Wang XD, Chen Y, Wu GJ, Tang YC et al. Ultrasensitive hybrid MoS_2-ZnCdSe quantum dot photodetectors with high gain. *ACS Appl Mater Interfaces* **11**, 23667–23672 (2019).
33. Ahn S, Chen WJ, Moreno-Gonzalez MA, Lockett M, Wang JY et al. Enhanced charge transfer and responsivity in hybrid quantum dot/graphene photodetectors using ZnO as intermediate electron-collecting layer. *Adv Electron Mater* **6**, 2000014 (2020).
34. Ye GL, Gong YJ, Lin JH, Li B, He YM et al. Defects engineered monolayer MoS_2 for improved hydrogen evolution reaction. *Nano Lett* **16**, 1097–1103 (2016).
35. Li SS, Lin YC, Zhao W, Wu J, Wang Z et al. Vapor-liquid-solid growth of monolayer MoS_2 nanoribbons. *Nat Mater* **17**, 535–542 (2018).
36. Liu P, Zhu XQ, Feng C, Huang M, Li J et al. Enhanced p-type behavior in the hybrid structure of graphene quantum dots/2D-WSe_2. *Appl Phys Lett* **111**, 111603 (2017).
37. Cho H, Jeong SH, Park MH, Kim YH, Wolf C et al. Overcoming the electroluminescence efficiency limitations of perovskite light-emitting diodes. *Science* **350**, 1222–1225 (2015).
38. Ning ZJ, Gong XW, Comin R, Walters G, Fan FJ et al. Quantum-dot-in-perovskite solids. *Nature* **523**, 324–328 (2015).
39. Cho IW, Ryu MY. Enhancement of luminescence properties and stability in perovskite hybrid structure with CdSe/ZnS quantum dots. *APL Mater* **7**, 051112 (2019).
40. Cho IW, Ryu MY. Effect of energy transfer on the optical properties of surface-passivated perovskite films with CdSe/ZnS quantum dots. *Sci Rep* **9**, 18433 (2019).
41. Lanzafame JM, Miller RJD, Muenter AA, Parkinson BA. Ultrafast charge-transfer dynamics at tin disulfide surfaces. *J Phys Chem* **96**, 2820–2826 (1992).
42. Shi HY, Yan RS, Bertolazzi S, Brivio J, Gao B et al. Exciton dynamics in suspended monolayer and few-layer MoS_2 2D crystals. *ACS Nano* **7**, 1072–1080 (2013).
43. Liu B, Zhao WJ, Ding ZJ, Verzhbitskiy I, Li LJ et al. Engineering bandgaps of monolayer MoS_2 and WS_2 on fluoropolymer substrates by electrostatically tuned many-body effects. *Adv Mater* **28**, 6457–6464 (2016).
44. Mak KF, He KL, Lee C, Lee GH, Hone J et al. Tightly bound trions in monolayer MoS_2. *Nat Mater* **12**, 207–211 (2013).
45. Suh J, Park TE, Lin DY, Fu DY, Park J et al. Doping against the native propensity of MoS_2: degenerate hole doping by cation substitution. *Nano Lett* **14**, 6976–6982 (2014).
46. Ross JS, Wu SF, Yu HY, Ghimire NJ, Jones AM et al. Electrical control of neutral and charged excitons in a monolayer semiconductor. *Nat Commun* **4**, 1474 (2013).
47. Mouri S, Miyauchi Y, Matsuda K. Tunable photoluminescence of monolayer MoS_2 via chemical doping. *Nano Lett* **13**, 5944–5948 (2013).
48. Li L, Wang WK, Chai Y, Li HQ, Tian ML et al. Few-layered PtS_2 phototransistor on h-BN with high gain. *Adv Funct Mater* **27**, 1701011 (2017).
49. Island OJ, Blanter SI, Buscema M, van der Zant HSJ, Castellanos-Gomez A. Gate controlled photocurrent generation mechanisms in high-gain In_2Se_3 phototransistors. *Nano Lett* **15**, 7853–7858 (2015).

Acknowledgements

This work is supported by National Natural Science Foundation of China (No. 92163135, 11904098, 51972105, U19A2090 and 62090035), Hunan Provincial Natural Science Foundation of China (No. 2019JJ30004), Hunan International Innovation Cooperation Platform (No. 2018WK4004), and Key Program of Science and Technology Department of Hunan Province (Nos. 2019XK2001, 2020XK2001).

Author contributions

Z. W. Li, W. Yang, A. L. Pan developed the original concept. Z. W. Li, X. Yang, C. G. Zhu designed and fabricated optoelectronic devices. W. Yang, M. Huang, C. L. He, L. H. Li performed optical experiments. Y. J. Wang, Y. F. Xie, Z. R. Luo, D. L. Liang, J. H. Huang, X. J. Zhuang contributed to the development of the experiment. X. L. Zhu, Z. W. Li, D. Li, A. L. Pan contributed to the writing of the manuscript. Z. W. Li and A. L. Pan supervised the research.

Competing interests

The authors declare no competing financial interests.

Supplementary information

Supplementary information for this paper is available at https://doi.org/10.29026/oea.2021.210017